

Progress of Atom Probe Tomography Analysis on Specific Grain Boundaries and Interfaces in Steel

Jun TAKAHASHI*
Yukiko KOBAYASHI
Kyohhei ISHIKAWA

Kazuto KAWAKAMI
Jun HAGA
Naoyoshi KUBOTA

Abstract

The segregation of alloying and impurity elements into grain boundaries and interfaces in steel significantly influences microstructure formation through recrystallization and transformation. It is very important to understand the phenomena by actual analysis of the segregation. Atom probe tomography (APT) enables a quantitative analysis of all elements that segregate at the boundary, however crystallographic information such as the boundary character could not be obtained by using APT alone. Therefore, we developed a new technique for the investigation of the boundary character using field ion microscopy (FIM) where the same needle tip as APT is used. This in-situ method determines the boundary character by fitting crystallographic poles into a FIM image. Furthermore, it also enables determination of the boundary plane by combination with an APT 3D elemental map and FIM analysis. We demonstrate APT analyses of recrystallized/unrecrystallized interfaces and prior austenite grain boundaries by applying the techniques to the needle tip fabrication process.

1. Introduction

As high strength steel consists of complicated microstructures, understanding such characteristic microstructures is necessary to obtain the desired properties of the material design for steels. The segregation of alloying and impurity elements into grain boundaries and interfaces in steel significantly influences microstructure formation through recrystallization and transformation. It is very important to understand the phenomena by actual analysis of the segregation into grain boundaries and interfaces. The segregation into grain boundaries and interfaces is considered to be a single or a few atomic layers in thickness, so quantitative observation of the segregation is very difficult. Even so, segregated elements that affect the embrittlement of grain boundaries have been analyzed on the fracture surfaces of grain boundaries by Auger electron spectroscopy (AES) for many years.¹⁾ However, this method requires fracture surfaces, so observable materials and grain boundaries are limited. Therefore recently, secondary ion mass spectrometry (SIMS) and transmission electron microscopes (TEMs) have been used to observe elements

segregated into grain boundaries and interfaces.^{2,3)} However, as it is difficult to observe some element groups by these analysis methods, a new quantitative analysis technique that can observe all segregated elements of lower concentration was required.

In the 1990s, three-dimensional atom probes were developed. In the 2000s, the atom probes became practical technique in atomic-scale elemental analysis by the innovation of technologies such as increasing the probing rate and enhancing the analysis volume. In this paper, such analysis method of the three-dimensional atom probes is referred to as atom probe tomography (APT). In addition, focusing ion beam (FIB) equipment has made it possible to fabricate needle specimen tips in a well-controlled manner, and APT is widely used to observe segregation at grain boundaries and interfaces.⁴⁾ APT can observe all segregated elements in one measurement with very high spatial resolution of a level of lattice spacing and good detection limit of 10 at ppm, although this depends on the measurement conditions. However, APT can measure only 200 nm at the tip of a needle specimen, so the target area must be included in the tip

* Chief Researcher, Dr. Eng., Materials Characterization Research Lab., Advanced Technology Research Laboratories
20-1 Shintomi, Futtsu City, Chiba Pref. 293-8511

apex. We developed a technique for fabricating needle specimen tips of specific regions and established observations of site-specific regions in the first half of 2000: In the new technique, a 10- μm block including a target area is extracted by the lift-out method while the microstructure is being observed by a scanning electron microscope (SEM) or other device; the block is placed on the needle post, and then fabricated by FIB milling to create a needle tip.⁴⁾

The grain boundary character affects the concentration of segregated atoms. For example, some researchers have reported that the segregation amounts at low angle grain boundaries are smaller than those at high angle grain boundaries.^{5,6)} The grain boundary character is determined by five parameters—five macroscopic degrees of freedom (DOFs): They are described as misorientation angle, rotation axis, and orientation of the grain boundary plane.⁷⁾ Many researches have been conducted on the relationship between segregation amount and grain boundary character. Suzuki, et al. reported that the amounts of P segregated into grain boundaries depend more on the grain boundary plane orientations than the misorientation angles.⁸⁾

In the observation of grain boundaries and interfaces, simply measuring segregated elements is not sufficient, but segregation amounts need to be discussed along with the grain boundary character. Although electron backscatter diffraction (EBSD) pattern analysis is widely used, we have developed a grain boundary characterization method using FIM analysis⁹⁾ as a simpler method. In this method, the misorientation angle and rotation axis are determined “in-situ” from the observation of field ion microscopy (FIM) images of a needle tip just before APT measurement. In addition, we have further improved this technique.¹⁰⁾ In the improved technique, the grain boundary plane can be determined by combining the in-situ FIM analysis with 3D element maps obtained from APT measurement. Using the “in-situ” FIM analysis technique to judge the grain boundary character when creating a needle tip has enabled observation of prior austenite (γ) grain boundaries and specific interfaces that used to be difficult to observe by APT. This paper introduces actual examples of quantitative observation of segregation states at recrystallized/unrecrystallized interfaces and prior austenite grain boundaries as application to steel materials.

2. Analysis of Crystal Orientation by FIM Analysis

APT is very useful for observing the distribution of alloying elements in atomic scale, but it is difficult to obtain crystallographic information on crystal structures and orientations only by APT. This is because the atomic positions measured by APT include errors caused by evaporation aberration and errors in 3D reconstructing. Some researchers have reported that the extent of the errors is up to 0.1 nm in the depth direction and up to 0.5 nm in the lateral direction, although they depend on the type of element.¹¹⁾ In diffraction methods by X-ray and TEM, diffraction patterns from entire crystal lattices are measured, so the crystal structure can be determined accurately. Meanwhile, in APT, the original positions are calculated from the positions where the field-evaporated ions arrived on the detector, so its accuracy is lower. FIM projects the atom positions on the tip surface using field-ionized gas ions, so the distribution of electric field on the surface, i.e., information on the crystal structure expressed on the surface, can be obtained. FIM can obtain information on crystallographic structures that cannot be obtained by APT, so it is useful to use FIM with APT to complement each other.

In this study, FIB equipment with the lift-out method was used to fabricate needle specimen tips. Ga ions were irradiated at an ac-

celeration voltage of 30 kV to mill materials and observe SIM images. An energy compensated atom probe with a delay-line position sensitive detector was used for APT measurement and FIM observation.

2.1 Determination of the rotation angles of grain boundaries⁹⁾

Figure 1(a) describes a point projection showing the relationship between an FIM image and projection positions of field ions. Where, x is the distance between the center of the hemisphere cap at the tip of the needle specimen (\mathbf{O}) and the center of projection (\mathbf{O}'), r is the radius of the curvature of the hemisphere cap, θ is the projection angle, L is the distance of the projection position from the center on the screen (\mathbf{O}''). As shown in the figure, the projection position of the atom at \mathbf{P} on the surface of the needle tip on the screen varies depending on projection center \mathbf{O}' . x/r is a projection parameter. Stereographic projection is equivalent to projection from the position where $x/r=1$, i.e., $x=r$. Many experiments have shown that on actual FIM images, linear projection with $L=k\theta$ is the best approximation. Figure 1(b) shows the relationship between the distance on the screen (L) and the projection angle (θ) in this point projection when the projection center (\mathbf{O}') is changed. As the projection angle is larger, the differences from the best approximation (linear projection) become larger. When x/r is about 1.8, the difference is the smallest. This value is used for the calculation of pole positions to be described later.

Figure 2 shows the coordinate system used in this calculation. Letters X , Y , and Z refer to the 3D coordinates of the needle coordinate system (origin \mathbf{O}). Letters X' , Y' , and Z' refer to the 3D coordinates (origin \mathbf{O}) of the crystal coordinate system. $X'=[100]$, $Y'=[010]$, and $Z'=[001]$ are crystal axes for ferritic iron. Z -axis corresponds to the needle direction. X - and Y -axes are in parallel to X'' and Y'' of the screen. Where, \mathbf{P} corresponds to the pole (l, m, n). The misorientation angle of the target grain boundary was calculated in

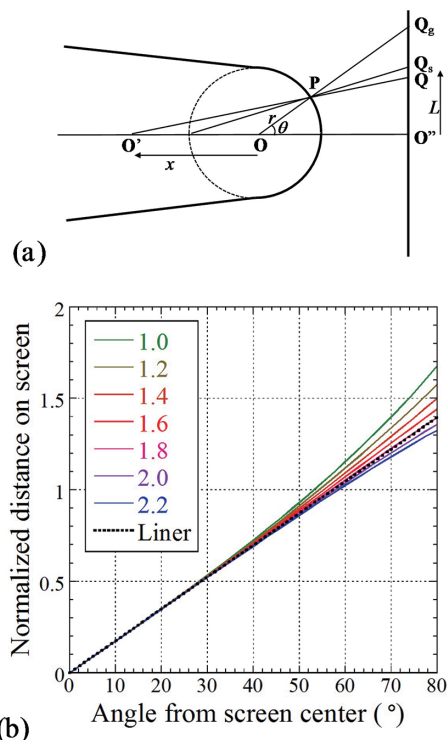


Fig. 1 (a) Schematic of FIM projections⁹⁾, (b) Relationship between central angle θ and normalized distance from the screen center L , calculated using various projection factors of x/r .⁹⁾

the following three steps by fitting of an actual FIM image.

First, orientation matrix **A** of crystal grain A, one of the two crystal grains composing a grain boundary, was calculated. This could be obtained by rotation to the crystal grain A's crystal coordinate system (*X'*, *Y'*, *Z'*) from the needle coordinate system (*X*, *Y*, *Z*). It was determined by fitting the calculated crystal orientation to the low-index pole positions in the actual FIM image. The pole positions were calculated by Euler angles (α , β , γ) and the distance between projection center **O'** and screen center **O''**. The distance to the screen center was adjusted using a scale parameter. To determine unique orientation here, at least three poles needed to be used for fitting. Pole-fitting was used for crystal grain B as well and orientation matrix **B** was calculated in a similar way. Then, the calculated two orientation matrices were matched by rotation. The rotation matrix was calculated using the formula below.

$$\mathbf{M} = \mathbf{B}\mathbf{A}^{-1} \quad (1)$$

Twenty-four coordinate transformation matrices \mathbf{R}_j ($j=1, 2, 3 \dots 24$) were applied to this formula to obtain 24 rotation matrices.

$$\mathbf{M}_j = \mathbf{R}_j\mathbf{B}\mathbf{A}^{-1} \quad (2)$$

Where, when rotation matrix elements are indicated as shown below,

$$\mathbf{M}_j = \begin{pmatrix} a_{11} & a_{12} & a_{13} \\ a_{21} & a_{22} & a_{23} \\ a_{31} & a_{32} & a_{33} \end{pmatrix} \quad (3)$$

the rotation axis and rotation angle of the grain boundary were calculated using the formulas below. The target grain boundary angle is

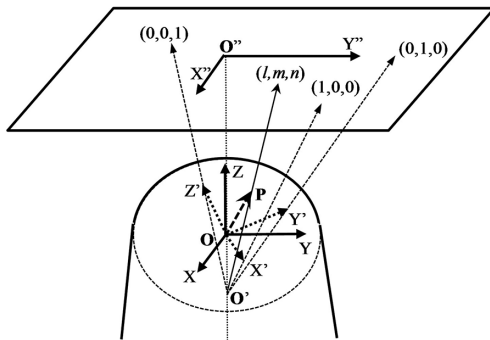


Fig. 2 Schematic of the coordinate systems
X, Y, and Z are the axes of the coordinate system fixed on the needle tip (the origin O). X', Y', and Z' are the axes of the crystalline coordinate system (the origin O). X'' and Y'' are the axes on the screen (the origin O'').⁹⁾

the smallest one in the rotation angles calculated with the 24 coordinates.

$$\phi_j = \cos^{-1} \left(\frac{a_{11} + a_{22} + a_{33} - 1}{2} \right) \quad (4)$$

$$\mathbf{I}_j = [I_{j1}, I_{j2}, I_{j3}] = \left[\frac{a_{23} - a_{12}}{2\sin\phi_j}, \frac{a_{31} - a_{13}}{2\sin\phi_j}, \frac{a_{12} - a_{21}}{2\sin\phi_j} \right] \quad (5)$$

Figure 3 shows the results of FIM analysis by this method in low-carbon ferritic steel.¹⁰⁾ The dark band indicated by the arrows in the FIM image is a grain boundary. The section enclosed with the broken lines is that measured by APT (Fig. 4). In this paper, the crystal grain in the top part of the needle tip is referred to as Grain-A and the crystal grain in the base part is referred to as Grain-B. As shown in the figure, the relatively definite poles of 002, 011, 211, and 310 in the FIM image were fitted on a PC screen to obtain the orientation matrices of the two crystal grains and then to calculate the rotation angle and rotation axis of the grain boundary. The smallest rotation angle was the misorientation angle of $\phi=20.4\pm 0.4^\circ$. The rotation axis was calculated by $\mathbf{I}=[0.713, -0.579, -0.394]$ in the needle coordinate system. This shows that this grain boundary is a random high-angle grain boundary. However, the orientation of the grain boundary plane that affects the segregation amount was not calculated in this method. In addition, the type of grain boundary was not shown.

2.2 Determination of orientation of grain boundary planes¹⁰⁾

The grain boundary for which the misorientation angle and rotation axis were determined by the FIM analysis was then measured by APT to obtain 3D elemental maps. Figure 4(a) shows elemental maps of Fe and C observed from the direction parallel to the grain boundary plane. Figure 4(b) shows the concentration profile obtained by a selected box ($10 \times 10 \times 30$ nm) cut out perpendicular to the boundary plane. At the grain boundary, C was segregated up to 7.8 ± 0.3 atom/nm² and P was segregated up to 0.28 ± 0.05 atom/nm² as interfacial excess.

How the grain boundary plane rotated to the reference plane of the 3D map coordinate system (e.g., plane Z) was estimated, and the normal grain boundary plane in the needle coordinate system was obtained by the rotation matrix. This was $\mathbf{n}=[-0.702, 0.428, 0.569]$ in the unit vector. The rotation axis vector in the same needle coordinate system was $\mathbf{I}=[0.713, -0.579, -0.394]$, so the angle between the normal vector of grain boundary plane and the rotation axis vector is $\theta=13.3^\circ$. This shows that the grain boundary's tilt component is 13.3° and twist component 76.7° , and thereby it is a mixed boundary with a high twist component. Thus, by examining the normal

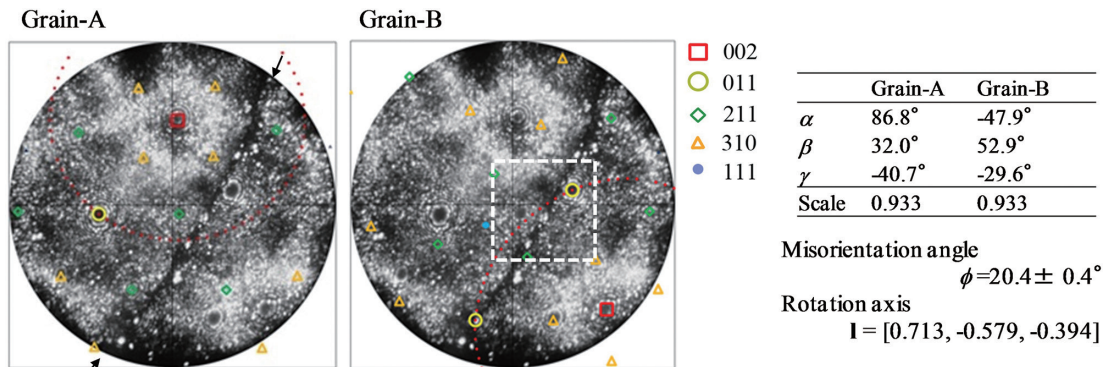


Fig. 3 Characterization of the grain boundary in ferritic steel using FIM pole-fitting method (needle coordinate)¹⁰⁾

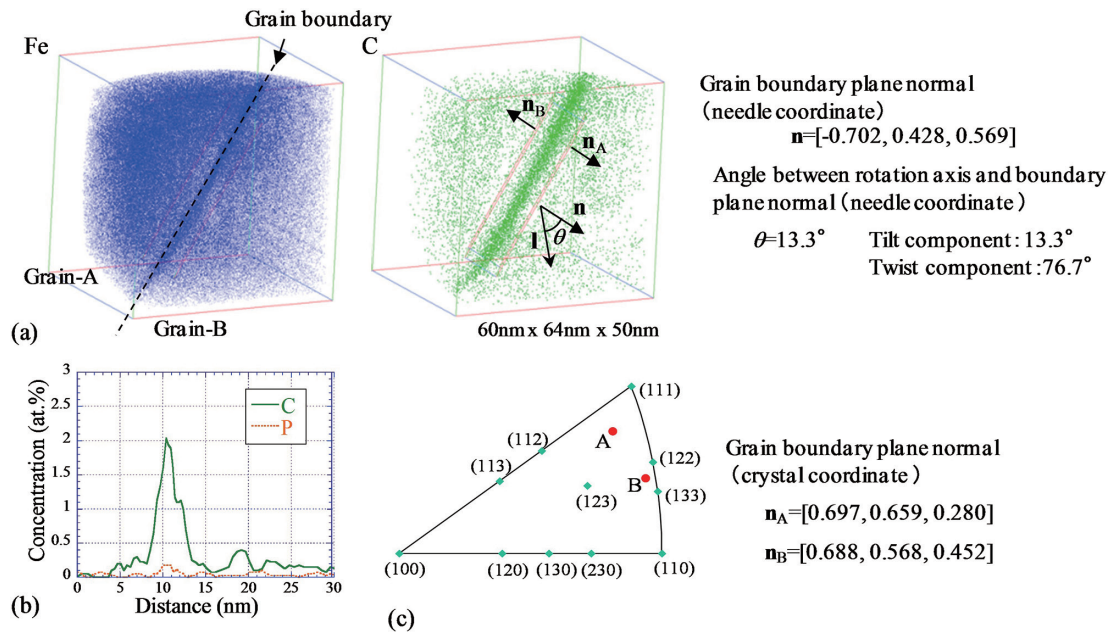


Fig. 4 Grain boundary characterization result¹⁰⁾

(a) 3D elemental maps, (b) Concentration profile, (c) Grain boundary plane normal in crystal coordinates of grain-A and grain-B

grain boundary plane, it is possible to investigate the type of grain boundary.

Next, the normal vector of grain boundary plane in each crystal coordinate system was calculated by coordinate transformation from the needle coordinate system to the two crystal coordinate systems. The vector for Grain-A was $\mathbf{n}_A = [0.697, 0.659, 0.280]$ and that for Grain-B was $\mathbf{n}_B = [0.688, 0.568, 0.452]$. These vectors show the orientation of the single grain boundary plane in the coordinate systems of the two crystal grains composing the grain boundary. When the value is equivalent to that of a low-index plane, it means that the energy of the interface is low. Figure 4(c) shows the orientation of the grain boundary planes in the crystal coordinates of Grain-A and Grain-B. This analysis shows that the two grain boundary planes (one close to [111] and the other at the center of the rotation from [111] to [110]) are random grain boundary planes.¹⁰⁾

2.3 Verification of accuracy⁹⁾

As described above, we have established a technique to study the character and type of grain boundaries. In this technique, our developed FIM analysis and APT analysis are complementarily used. No such in-situ FIM analysis was reported in the past and thereby how misorientation angles estimated by the FIM pole-fitting method are accurate remained unclear. Therefore, the ferritic steel sample for which strain had been removed by annealing was used to verify the accuracy of the estimated misorientation angle.

The angles of five grain boundaries were examined by EBSD first. Needle specimen tips were fabricated from those by the lift-out method and FIB milling. Their misorientation angles were determined by the FIM pole-fitting. For the five needle tips, the difference from the values estimated by EBSD in advance was at most 0.6° . EBSD measurement itself contains errors of 0.1 to 0.5° in determination of the orientation from the Kikuchi band at each measurement point. The results show that the angles estimated by pole-fitting were sufficiently accurate. However, if the cross section of a needle tip is elliptical, the accuracy lowers, so attention is required.

This method in which in-situ FIM analysis is used can examine needle tips for APT before the measurement, so it has an advantage

—FIM analysis results can be compared to APT measurement results directly in addition to judgment of target grain boundaries and interfaces. In addition, a misorientation angle close to a grain boundary (approximately 10 nm from a boundary) can be examined, so this method can accurately determine misorientation angles very close to grain boundaries in pearlitic steel and bainitic steel containing large strain in grain.

3. Progress of Techniques for Observing Specific Grain Boundaries and Interfaces

In the previous section, the FIM analysis techniques to examine the misorientation angle and orientation of grain boundary planes were demonstrated. In this section, as application of these techniques, APT analyses of recrystallized interfaces and prior austenite grain boundaries in steel were demonstrated. Such direct atomic-scale observations have been required in steel researches for a long time.

3.1 Observation of recrystallized/unrecrystallized interfaces¹²⁾

Haga et al. has reported that in ultra-low carbon steel containing solute Ti, the addition of a few mass ppm of B significantly retards the growth of recrystallization nuclei during annealing after cold rolling.¹³⁾ This phenomenon becomes conspicuous when solute Ti exists, so it was thought that it was caused by the interaction of B and Ti.¹⁴⁾ The solute drag effect is a mechanism that retards the growth of recrystallization nuclei. As the mechanism, alloying and impurity elements are segregated into recrystallized/unrecrystallized interfaces and when the interfaces move, they drag the segregated atoms and thereby the driving force is consumed, or the mobility is deteriorated. However, in the recrystallization temperature range, B itself diffuses faster than general substitutional atoms and thereby the drag effect is small. However, if Ti segregates into interfaces due to the attractive interaction between B and Ti, the solute drag effect could be high.¹⁴⁾ To verify this hypothesis, elements segregated into recrystallized interfaces were observed by APT.

In this experiment, ultra-low carbon interstitial free (IF) steel with 0.05 mass% Ti was used, where the amount of B addition var-

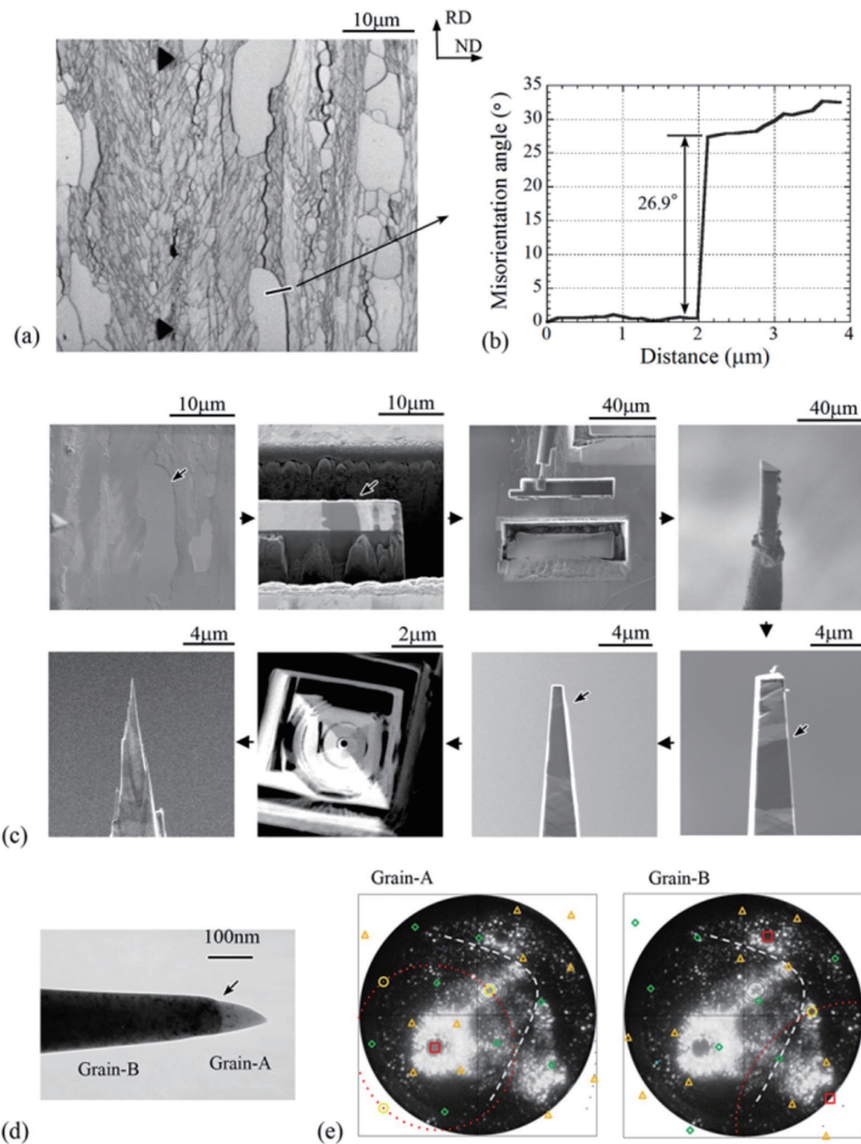


Fig. 5 Processes of needle tip fabrication and interface confirmation¹²⁾

(a) EBSD IQ map, (b) Misorientation angle of line profile across the aimed interface, (c) Needle tip fabrication of the interface by FIB milling with the lift-out method, (d) TEM micrograph of the tip after final milling, (e) Characterization of the interface by FIM pole fitting method

ied from 1 to 14 mass ppm. The steel was hot rolled and then heat treated at 700°C for 30 min equivalent to coiling to precipitate and scavenge contained N, C, and S with Ti. The amount of solid solution Ti (sol.Ti) was estimated to be about 0.03 mass%. After being rolled at the cold rolling ratio of 80%, the steel was recrystallization-annealed in a salt bath at 650°C for 30 s to six days to examine the progress of recrystallization. Sample steels without B (1B-4 min) and with 14ppm B (14B-60 min) in the early stage of recrystallization were used for observation.

Figure 5 shows the processes of needle tip fabrication for the observation of recrystallized/unrecrystallized interfaces. A target interface was selected from an EBSD map (Fig. 5(a)) and its misorientation angle was examined in advance (Fig. 5(b)). This is to avoid confusion by comparing with the value obtained by the FIM analysis prior to APT measurement of the needle tip because fine recovery crystal grains exist in the unrecrystallized region. A fine block ($10 \times 10 \times 30 \mu\text{m}$) including the target interface was extracted by the

FIB lift-out method and set to the needle post. The needle tip was fabricated by FIB such that the interface is located in the needle tip (approximately 100 nm from the tip apex) (Fig. 5(c)). The misorientation angle of the interface in the needle tip (Fig. 5(d)) was examined by the FIM pole-fitting method (Fig. 5(e)). The estimated angle was $27.9 \pm 0.4^\circ$, almost matching the value ($26.9 \pm 0.2^\circ$) obtained by the EBSD in advance. This result confirmed that it was the target recrystallized/unrecrystallized interface.

Figure 6 shows the results of the APT measurement of the needle tips obtained by this method. The broken lines in the 3D maps are the positions of the recrystallized/unrecrystallized interfaces. On the 1B-4 min steel without B, Ti segregated to some extent (up to 0.7 atom/nm²), although B hardly segregated. This means that there is attractive interaction, albeit small, between Ti and the interface.

On the other hand, on the 14B-60 min steel with B, B highly segregated (up to 4.1 atom/nm²) and Ti also segregated (up to 1.9 atom/nm²). Ti segregated into the steel without B, but the segrega-

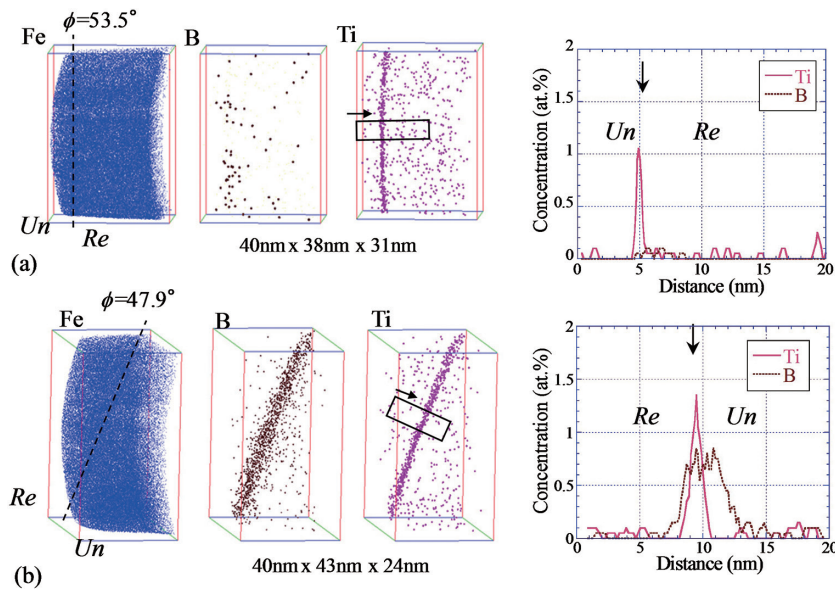


Fig. 6 3D elemental maps and concentration profile across the recrystallized/unrecrystallized interface in the steels⁹⁾
 (Re: recrystallized grain, Un: unrecrystallized grain, ϕ : misorientation angle)
 (a) Without B (1B-4 min), (b) With B (14B-60 min)

tion amount of Ti was increased by the addition of B. A similar trend was seen on grain boundaries for which recrystallization has completed. This shows that there is attractive interaction between B and Ti atoms and they are in a co-segregation relationship. From Cahn's solute drag model, the reason why the drag force increases by the addition of B is possibly because segregation of B into the interfaces enhanced the interaction energy between Ti and the interfaces. From actual changes in the Ti segregation concentration, when the segregation width is supposed to be 1 nm, the increased interaction energy between Ti and the interfaces due to the segregation of B is estimated to be approximately 0.1 eV.¹⁵⁾

3.2 Observation of prior austenite grain boundaries¹⁶⁾

By adding a minute amount of B, B segregates into austenite (γ) grain boundaries and suppresses the formation of ferrite nuclei, which improves hardenability. Some researchers have reported that the addition of Mo to such steel containing B further improves the hardenability. The mechanisms of the combined addition effect on the segregation to γ grain boundaries and the hardenability have been discussed.^{17,18)} To clarify the mechanisms, we quantitatively observed elements segregated to prior austenite grain boundaries by APT. The basic component is 0.15C-0.27Si-1.3Mn-0.02Ti-0.0007N (mass%) and to which 10 mass ppm of B and 0 to 1.0 mass% of Mo were added. Test pieces of the steels were heated at 950°C for 20 s to form austenite (γ) and were cooled to 650°C at various cooling rates, and then were quenched by He gas.¹⁹⁾

From EBSD measurement of the surface of sample steels, prior austenite grain boundaries were recognized as grain boundaries with misorientation angles other than the K-S (Kurdjumov-Sachs) relation. The lift-out method, FIB milling, and TEM observation were used to create a needle specimen tip that included the target prior austenite grain boundary in the tip apex (Fig. 7). In this experiment, the FIM pole-fitting method was used to examine the misorientation angles of grain boundaries in the tip before APT measurement to make sure that the grain boundaries were the target ones. In martensitic microstructure like these steels, lath, block and packet boundaries often exist, so recognizing prior austenite grain boundar-

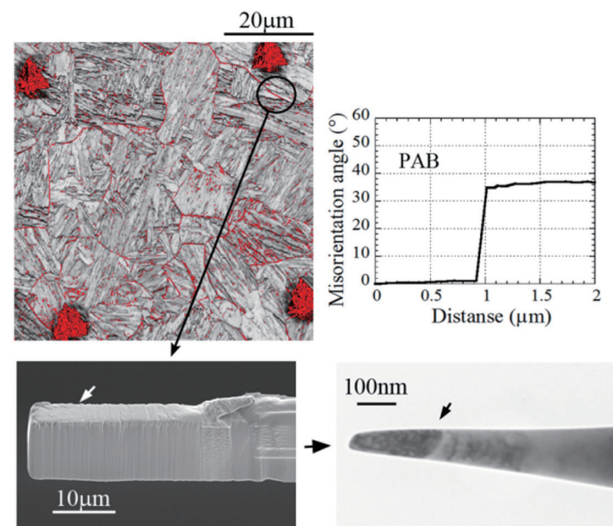


Fig. 7 Fabrication process of a needle tip containing the prior austenite grain boundary using combination of EBSD analysis and FIB lift-out method¹⁶⁾

ies before APT measurement and distinguishing them from lath, block and packet boundaries significantly improved the success rate of observation of prior austenite grain boundaries that was very difficult.

Figure 8 shows the results of APT measurement of prior austenite grain boundaries in steels with 10 mass ppm B and that were cooled from 950°C to 650°C at 30°C/s. B and C highly segregated into the prior austenite grain boundary in steel without Mo (Fig. 8(a)). B was homogeneously distributed to the entire grain boundary as a solid solution and no clusters formed on the grain boundary. On the other hand, B, Mo, and C highly segregated into the prior austenite grain boundary in steel with 1 mass% Mo (Fig. 8(b)). B and Mo segregated only at the prior austenite grain boundary and did not segregate into the martensite packet, block, and lath boundaries, but

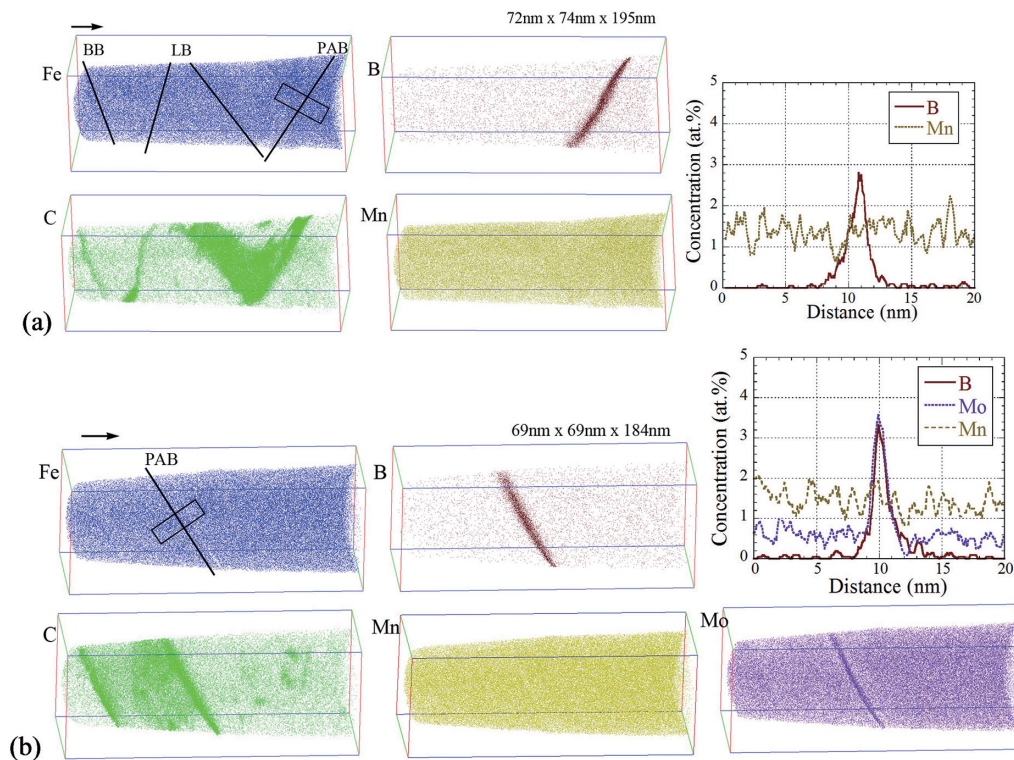


Fig. 8 3D elemental maps and concentration profiles at the prior austenite grain boundary in 10ppm B added steels without (a) and with 1 mass% Mo (b)¹⁶⁾ (Prior austenite grain boundary, packet boundary, block boundary, and lath boundary were represented as PAB, PB, BB, and LB, respectively.)

C segregated into all the boundaries formed by the martensite transformation. This means that C also diffused after the transformation, but B and Mo could not be diffused and retained the segregation state in the austenite before the transformation.

We studied how the cooling rate and the amount of added Mo affected the segregation amounts systematically using these techniques. Through this study, a quantitative model that explains the behavior of the segregation of B and Mo into austenite grain boundaries during cooling was proposed and the relationship between the grain boundary segregation amount and hardenability was clarified.¹⁶⁾ Austenite (γ) grain boundaries are nucleation sites for transformation and precipitation, and the segregation of the alloying and impurity elements plays an important role in microstructure formation. Our developed techniques need to be further utilized in the future.

4. Conclusion

We developed a new in-situ FIM analysis technique and established advanced APT analyses with higher reliability. This technique was applied to observe site-specific regions such as prior austenite grain boundaries and recrystallized/unrecrystallized interfaces in steels. Although steel has a long history of research, several unresolved issues remain. Such an atomic-scale characterization links industrial steel production and material science, further increasing its importance in the steel industry.

References

- 1) For example, Lejček, P.: Grain Boundary Segregation in Metals. Springer, Berlin, 2010
- 2) Tanaka, T., Hayashi, S.: Shinnittetsu Sumikin Giho. (408), 26 (2017)
- 3) Shigesato, G., Taniguchi, S., Sugiyama, M., Ikematsu, Y.: Shinnittetsu Giho. (390), 8 (2010)
- 4) Takahashi, J., Kawakami, K., Kobayashi, Y., Yamada, J.: Shinnittetsu Giho. (390), 20 (2010)
- 5) Maruyama, N., Smith, G.D.W., Cerezo, A.: Mater. Sci. Eng. A353, 126 (2003)
- 6) Herbig, M., Raabe, D., Li, Y.J., Choi, P., Zaefferer, S., Goto, S.: Phys. Rev. Lett. 112, 126103 (2014)
- 7) Cahn, J.W.: J. Phys.-Paris. 43, 199 (1982)
- 8) Suzuki, S., Abiko, K., Kimura, H.: Scripta Metall. 15, 1139 (1981)
- 9) Takahashi, J., Kawakami, K., Kobayashi, Y.: Ultramicroscopy. 140, 20 (2014)
- 10) Takahashi, J., Kawakami, K., Kobayashi, Y.: CAMP-ISIJ. 27, 457 (2014)
- 11) Blavette, D., Duval, P., Letellier, L., Guttman, M.: Acta Mater. 44, 4995 (1996)
- 12) Takahashi, J., Haga, J., Kawakami, K., Ushioda, K.: Ultramicroscopy. 159, 299 (2015)
- 13) Haga, J., Mizui, N., Nagamichi, T., Okamoto, A.: ISIJ Int. 38, 580 (1998)
- 14) Haga, J., Sawada, S., Ushioda, K.: Tetsu-to-Hagané. 103, 221 (2015)
- 15) Takahashi, J., Haga, J., Kawakami, K., Ushioda, K.: CAMP-ISIJ. 28, 318 (2015)
- 16) Takahashi, J., Ishikawa, K., Kawakami, K., Fujioka, M., Kubota, N.: Acta Mater. 133, 41 (2017)
- 17) Ueno, M., Ito, K.: Tetsu-to-Hagané. 74, 1073 (1988)
- 18) Asahi, H.: ISIJ Inter. 42, 1150 (2002)
- 19) Ishikawa, K., Nakamura, H., Homma, R., Fujioka, M., Hoshino, M.: ISIJ Inter. in press (2018)

NIPPON STEEL & SUMITOMO METAL TECHNICAL REPORT No. 118 MARCH 2018



Jun TAKAHASHI
Chief Researcher, Dr. Eng.
Materials Characterization Research Lab.
Advanced Technology Research Laboratories
20-1 Shintomi, Futtsu City, Chiba Pref. 293-8511



Jun HAGA
Senior Researcher
Sheet & Coil Research Lab.
Steel Research Laboratories



Kazuto KAWAKAMI
Dr. Eng.
Nippon Steel & Sumikin Technology Co., Ltd.



Kyohhei ISHIKAWA
Plate & Shape Research Lab.
Steel Research Laboratories



Yukiko KOBAYASHI
Senior Researcher
Materials Characterization Research Lab.
Advanced Technology Research Laboratories



Naoyoshi KUBOTA
Dr. Eng.
Nippon Steel & Sumikin Technology Co., Ltd.